Wavefront Control for the Next Generation Space Telescope

David Redding, Scott Basinger, Andrew E. Lowman, Fang Shi
Jet Propulsion Laboratory, California Institute of Technology

Pierre Bely
Space Telescope Science Institute

Richard Burg
Johns Hopkins University

Gary Mosier
Goddard Space Flight Center, National Aeronautics and Space Administration

ABSTRACT

The Next Generation Space Telescope will abandon the traditional means of providing high optical quality and stability, namely use of massive structures. Instead, a benign orbital environment will provide stability for a large, flexible, lightweight deployed structure, and active wavefront controls will compensate misalignments and figure errors induced during launch and cool-down on orbit. This paper presents a baseline architecture for NGST wavefront controls, including initial capture and alignment, segment phasing, wavefront sensing and deformable mirror control. Simulations and analyses illustrate expected scientific performance with respect to figure error, misalignments, and thermal deformation.

1.INTRODUCTION

The Next Generation Space Telescope (NGST) will be a large-aperture, extremely light weight, cryogenic, infra-red space telescope, providing imagery and spectrometry from 1 um to 16 um wavelength.[1-2] It will be diffraction limited at a wavelength of 2 um. With an aperture of about 8 m, NGST will provide about ten times the collecting area of the Hubble Space Telescope, in a package that weighs only 3500 kg and fits into the shroud of a small expendable launch vehicle. It will operate far from Earth, in a halo orbit or a sun-centered orbit, where the thermal and dynamical environment is benign.

NGST will be subject to disturbances from a variety of sources. Those that impact imaging performance include optical manufacturing errors, thermal deformations, shifts in alignments during launch, deployment errors, and spacecraft-induced vibrations. To compensate these effects, and to perform initial alignment of the telescope following launch, NGST will be equipped with a wavefront control system.

This paper examines the architecture and performance of the optical control system for the NGST "Yardstick" design. The Yardstick is a point design developed by a team led by the Goddard Space Flight Center. It is intended to provide context and focus for the NASA team, to help in evaluating feasibility and performance of NGST, to identify new technology requirements, to resolve technological issues, and to prepare the government team for the procurement of the NGST spacecraft. Several other designs are also under active study by industry, NASA and ESA teams.[1]

The Yardstick, like most proposed NGST designs, uses deployed, segmented primary mirror optics and a deployed secondary mirror. A large sunshield shades the spacecraft, allowing it to cool passively to cryogenic temperatures (Fig. 1). Orbiting around the Earth-Sun L2 point, the thermal and dynamical environment is benign, providing for a high degree of passive stability once the spacecraft has cooled to operational temperatures. Figure and alignments are held passively during observations.

The immediate post-launch, post-deployment condition of the NGST optics will be poor. Segment figure will have changed significantly during cooling from ambient to orbital temperatures. If this is not predicted and compensated precisely, residual wavefront error of a few waves will be induced. The segments will have figure error residuals from the fabrication process. Segments and the SM may be misaligned by millimeters and milliradians. Initially, there may be no light on the focal plane.

The first task for the NGST wavefront control system is therefore to acquire and align the secondary and primary segments to the science instruments. This is accomplished by a "coarse figure initialization" controller. Using the Near IR science imaging camera observing an isolated bright unresolved star, the

segments are aligned individually to the SM and Integrated Science Instrument Module (ISIM), to within a few 10s of microns of its ideal configuration. Then the segments are cophased, using spectrally-dispersed interference fringes formed by a grism in the NIR camera filter wheel, and using imagery in a white-light interferometry mode.

This coarse initialization process is expected to be needed only once, at the beginning of the mission. It will leave the primary mirror aligned and phased to within a few waves residual error at the target 2 um wavelength. The amount of error here is largely a function of the optical quality of the segments.

"Fine initialization control" occurs following coarse phasing at the beginning of the mission, and then periodically throughout the mission (Fig. 2). Wavefront sensing is performed using defocussed imagery from NIR and Far IR cameras. The baseline sensing approach uses a focus-diverse phase retrieval algorithm to estimate the phase across the pupil. This estimated wavefront is processed to determine optimal segment and deformable-mirror (DM) commands, which are then implemented. This process is iterated until the performance objective is met.
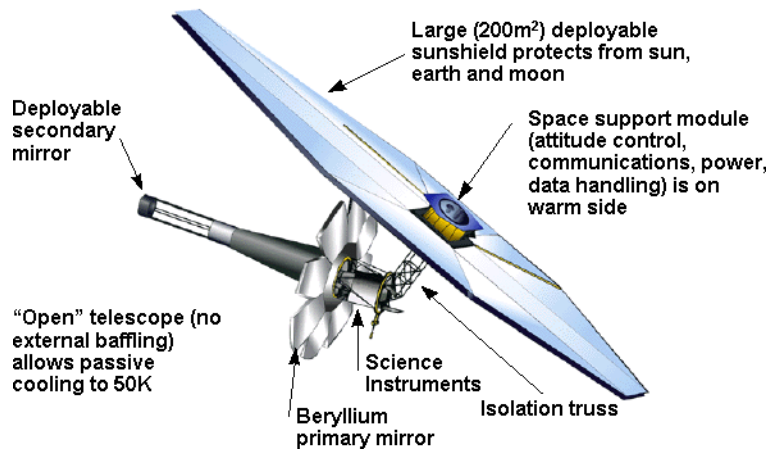
Figure 1. The NGST Yardstick configuration.

The baseline WF control does not operate during scientific operations. Passive structural stability is relied on to hold figure and alignment during this period.

Telescope guiding uses a combination of the spacecraft attitude control system and fast-steering mirror (FSM) control. The FSM is driven at a 100 Hz refresh rate, using an opportunistic guide star windowed in one section of the NIR camera focal plane. Predicted jitter, assuming the telescope is aligned, is under about 1/10th of a pixel, at a few milliarcsec.[3] In the initial phases of alignment, the FSM is not used, as there is not an adequately sharp image for focal-plane guiding. Instead, the spacecraft ACS provides star-tracker referenced pointing, which is noisier and slowly drifting. Fast exposures of bright stars minimize the effects of jitter in this phase. Full guiding begins when the center segment is reasonably well aligned, so that a usable off-axis star image can be obtained.
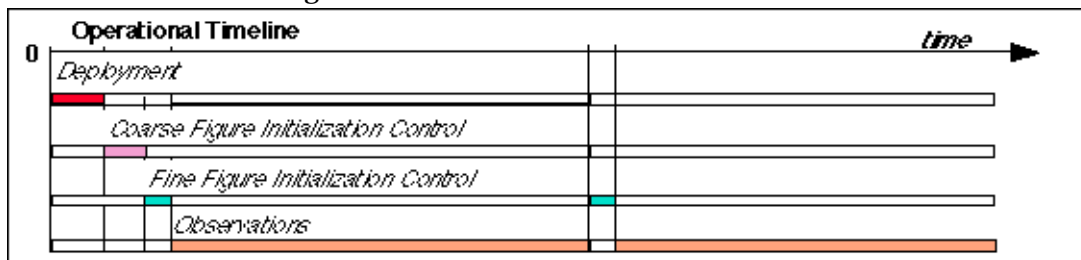

Figure 2. Wavefront control timeline.

This paper describes the control approach in a bit more detail, and then illustrates its operation with a couple of specific examples. Performance with respect to the major sources of errors is then quantified. It is shown that the wavefront controls permit significant relaxation of mirror figure error tolerances in the low

spatial frequencies. Deployment errors and other misalignments are also easily compensated. Expected thermal response, from ground to orbit, and then between operational extremes, is near mission objectives.

Wavefront control performance is a direct function of disturbing factors from every subsystem of the spacecraft. To evaluate this performance completely requires treating the NGST OTA, SSM and SIM as an integrated dynamical system. This is done using "IMOS," a computer modeling environment that combines finite-element structures models with ray-trace and diffraction-based optics, heat-transfer models, as well as a full spacecraft attitude control system.[3] Dynamical performance, including jitter effects on the optics is dealt with in Ref. 3. The discussion here assumes stable guiding, which allows treatment of the WF control problem as a quasi-static process.

2.SYSTEM DESCRIPTION

The NGST Yardstick utilizes 9 segments in a "flower" pattern to form its primary mirror (Figs. 1 and 3). The center segment is hard-mounted to the ISIM structure. The outer segments are folded – some up, some down – to fit into the launch vehicle shroud. Once on orbit, they deploy, each in a single rotation. The SM is mounted on a deployed 4-strut tower, attached to a conical baffle. The mirrors and support structures are made of beryllium. The SM is followed by small tertiary and quartenary mirrors (Fig. 3); the latter is a deformable mirror (DM). This is followed by a fast-steering mirror (FSM). The NIR camera optics include a pyramid mirror, which feeds 4 separate channels of the NIR camera, and an Offner relay, which directs the light to the detector. More complete descriptions of the optical layout are provided in Refs. 1 and 9. Figure 4 illustrates the PSF obtained with perfect optical quality.
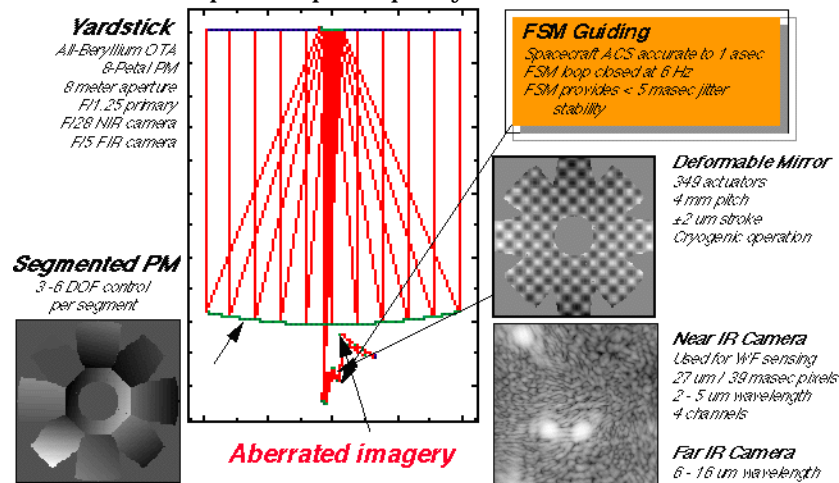

**Figure 3. NGST Yardstick layout, pupil map, and aberrated image.**

The deformable mirror is placed at a pupil image, which is about 80 mm wide. It uses a 349-actuator format, on a 19-by-19 grid at about 3.8 mm spacing (Fig. 5), and a ±2 um stroke capability. This performance is achievable at ambient temperatures, but have not been demonstrated at cryogenic temperatures. It is expected that an appropriate tailoring of materials in the actuators will produce a good cryogenic DM.

Figure 5 illustrates the DM actuator influence function assumed in the Yardstick performance studies. This function was derived assuming a membrane supported by a discrete grid of compliant actuators. Other influence functions, especially measured ones, are easily substituted. The 349-actuator mirror was chosen because it is a standard format, albeit with somewhat finer pitch than usual. It remains to determine the optimal DM actuator density and stroke. This requires a complex trade of DM stroke vs. pupil size and actuator spacing, given particular PM segment manufacturing processes and errors.Use of deformable primary mirror segments is an attractive option from the control engineer's point of view, and is a feature of some of the industry proposals. There is value in removing aberration at the point it is induced, especially for a wide field system. The DM is very effective on-axis, but the correction degrades with field angle, as the mapping from the PM to the DM distorts slightly. The second reason to bend the PM is to

match segment edges better, which makes the continuous facesheet DM more effective. A relatively small number of PM actuators could accomplish the latter without unduly complicating the mechanics of the PM segment deployment. For a high actuator density system, the compactness, light weight and relatively uncomplicated cabling make the DM attractive.
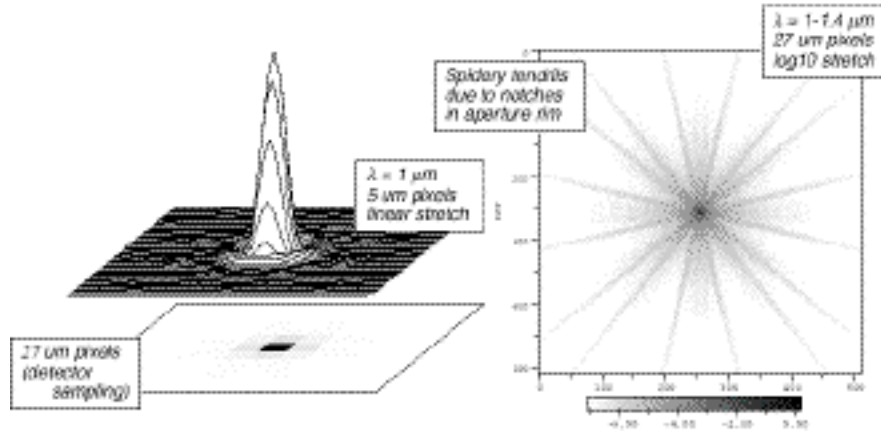
Figure 4. Nominal point-spread function.
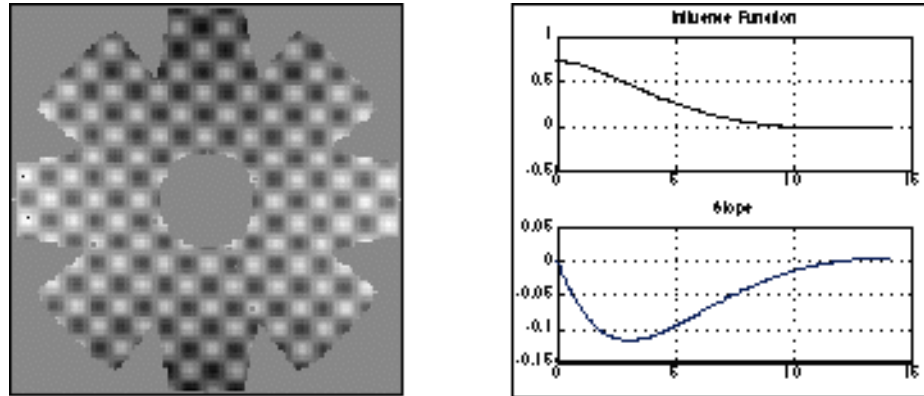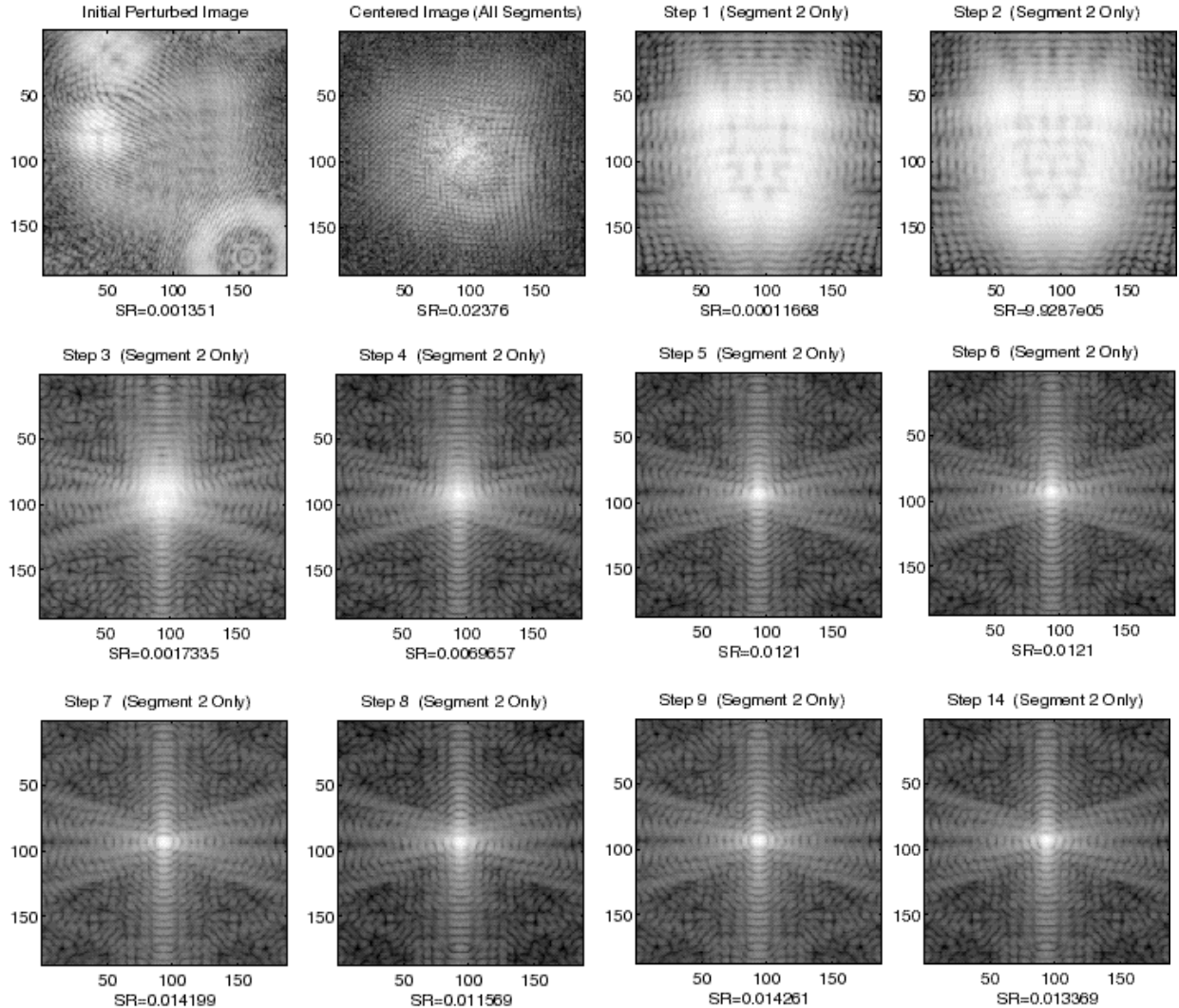

Figure 5. Deformable mirror.

3.CAPTURE AND COARSE ALIGNMENT

The baseline NGST optical controller has 2 major modes: Coarse Initialization Control, wherein the initial alignment and phasing of the telescope is performed; and Fine Initialization Control, wherein the 9 primary mirror (PM) segments, the secondary mirror (SM), and the deformable quartenary mirror (DM) are set together so as to minimize wavefront error (WFE) and maximize Strehl ratio (SR) for the ensuing observations. Coarse Initialization Control is itself split into 2 modes, the first of which is Capture and Coarse Alignment, described in this section. The second main mode of the Coarse Initialization Control is the Coarse Phasing Control, discussed in the next section.

Capture and Coarse Alignment begins at first light, following the initial deployment of the primary and secondary mirrors. The telescope is pointed at an isolated bright star, and the first pictures are taken by the Near IR camera. An example of what might be expected is shown in the upper left frame of Fig. 6, which shows the image of a single bright star taken with the primary mirror misaligned by random errors. The misalignments have standard deviations of 300 umin translation and 10 urad in tilt. As shown, only a few of the 9 segments reflect light onto the focal plane; the others are so misaligned as to send their spots off of the detector field of view. Those spots that do fall on the detector are blurred by defocus, showing fuzzy outlines of the the segment shapes.

It is the task of the Capture controller to identify which spots correspond to which segment, including those that fall off of the detector initially. It then aligns and focusses each segment individually to the

4

Integrated Science Instrument Module (ISIM) and SM. The center segment is aligned first, and then used as a reference to which all other segments are aligned. Guiding begins once the center segment is captured and focussed.

| Initial Perturbed Image	Centered Image (All Segments)	Step 1 (Segment 2 Only)	Step 2 (Segment 2 Only)
SR=0.001351	SR=0.02376	SR=0.00011668	SR=9.9287e05
Step 3 (Segment 2 Only)	Step 4 (Segment 2 Only)	Step 5 (Segment 2 Only)	Step 6 (Segment 2 Only)
SR=0.0017335	SR=0.0069657	SR=0.0121	SR=0.0121
Step 7 (Segment 2 Only)	Step 8 (Segment 2 Only)	Step 9 (Segment 2 Only)	Step 14 (Segment 2 Only)
SR=0.014199	SR=0.011569	SR=0.014261	SR=0.013369

Figure 6. Capture and alignment example, showing initial image and images taken during the process of focussing Segment 2.

The capture process proceeds as follows for each segment:

1. Identifying segment spots that fall on the detector. A reference image is taken, and then the segment is moved a small amount, and a second frame is taken. The 2 frames are registered and differenced. The difference frame is compared to a detection threshold. If the difference is not significant, then the segment spot is not on the detector. If the illumination difference is significant, the difference frame is centroided to determine the location of the segment spot. The segment is then tilted to move its spot to the center of the field. This process is repeated for each segment.

2. Scanning to find segments spots that are initially off the detector. The segment is scanned in a regular pattern (cone, raster, etc.) in increments of angle slightly smaller than the detector FOV. After each tilt, a frame is taken, registered to the reference frame and thresholded. If a new spot is detected, it is centroided and driven to the appropriate point. If no new spot is detected, the next scan step is taken and the process is repeated. The scan proceeds until each segment spot is detected and centered. At this point the image will look something like the second frame in Fig. 6, a big diffuse blob in the center of the detector.

3. Segment focussing. For each segment, begins by moving all other segment spots away from the center to assigned locations in the FOV. Step 1 is to take a first frame showing the defocussed, centered image of the subject segment, as shown in Fig. 6. The segment is then moved slightly in focus, and a second frame is taken (Step 2). The encircled energy within a large circle radius (30 pixels initially) is computed for each frame. This is used to determine whether the small step moved towards or away from focus, and to determine the size of the next step. The next step is implemented and the process is repeated. Recentering is done after large steps. If the encircled energy exceeds a certain threshold, a smaller energy circle is used. The radii of the energy circles for the focussing metric are different for the central and outer segments. For the example they were 30, 15 and 3 pixels for outer segments; the central segment radii were 40, 20 and 3. For defocus errors, more sets of larger radii may be desirable. The process converges when the maximum encircled energy within the smallest circle is found.

Figure 6 shows the images taken during this process for our example. The encircled energy metrics used at each step are shown in Fig. 7. The numbers correspond to the images in Fig. 6. This example took 9 steps to converge, though 5 additional ones did result in a slight improvement.
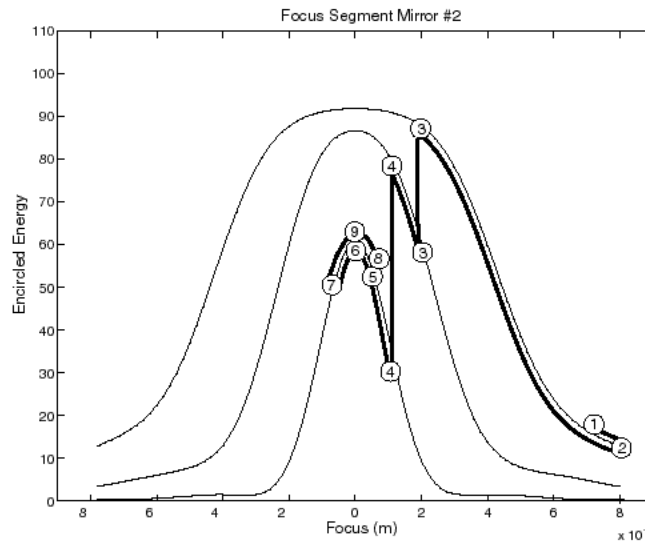

Figure 7. Encircled energy for 3 different radii during segment 2 focussing example.

Following the focussing of the center segment, and before focussing the other segments, alignment of the center segment to the SM and ISIM is accomplished. This is done with the outer segments masked or tilted out of the line of sight. It utilizes "prescription retrieval" software called VSIM, which processes defocussed narrow or broad-band imagery to directly estimate misalignment and low-order figure error terms.[4,5,6] VSIM has been successfully applied to several different instruments, starting with the Hubble Space Telescope and including several other space instruments, tested in situ or on the ground. With appropriately diverse data VSIM is capable of separating the effects of misalignments from those of figure errors, and can distinguish between figure errors on multiple surfaces. Experience indicates that VSIM will enable alignment of the center segment and SM to the ISIM to within a few μm and μrad.

The capture and alignment process is then repeated for each of the outer segments, though using a different, slightly off-axis field of view for each, so as not to interfere with the light from the central segment. At the conclusion of this process, each segment is aligned to within a few μm and μrad. Figure 8 summarizes performance of our example, with the rightmost frames showing the image and WF after each segment is focussed and brought back into the center of the frame. WF error went from nearly 1 mm at first light to 16 μm – well within the capture range of the Coarse Phasing controller described next.

Total dynamic range for the Capture controller is expected to be quite large, several mm in focus and tens of minutes to degrees in angle. The Capture process is aided by the large detector array (4 minutes on a side) planned for the Near IR camera. Solutions to certain complicating factors, such as confusion from

multiple objects in the field, mirror aberrations, and image registration during periods of poor guiding remain to be engineered, but no fundamental obstacle exists.
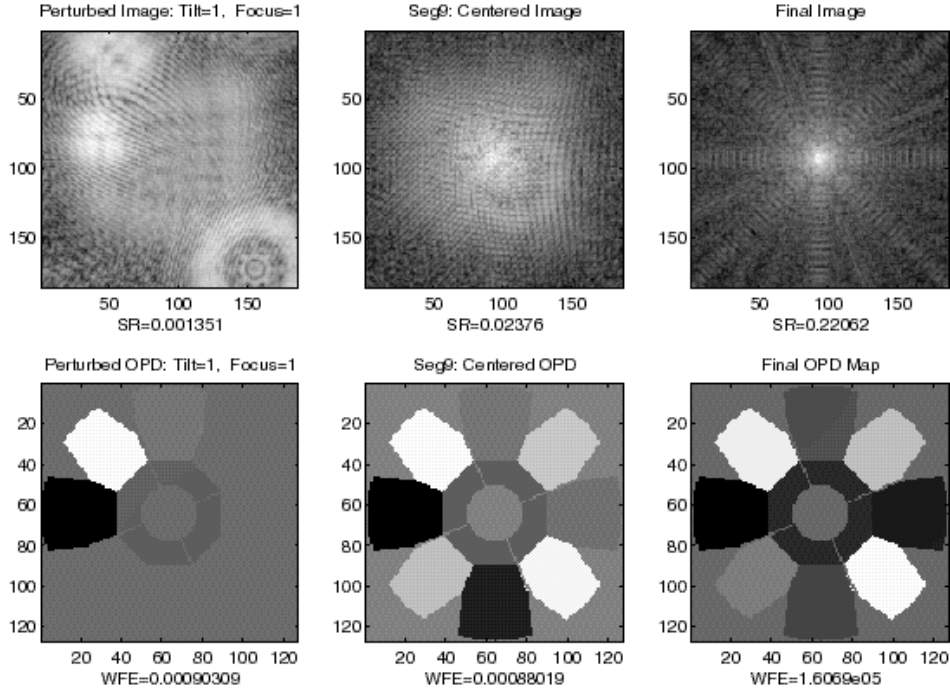
Figure 8. Wavefront error for capture example: initially; following capture; and following coarse focussing.

4. COARSE PHASING

Now begins the coarse phasing process. First, the 8 outer segments are tilted out to point at specific spots well outside the center of the CCD. Each outer segment is then tilted back in, one at a time, and coaligned with the center segment, so that their 2 spots overlie. The 2 segments are not in phase at this point, with perhaps a few microns difference between them. To detect this phase difference, a prism or grism may be placed in the beam, creating a "dispersed-fringe sensor" (DFS) as illustrated on Fig. 9. The DFS disperses the light from the 2 coaligned segments up and down the detector, so that the light at any point on the detector is at a single wavelength. Phase differences between the 2 segments cause the overlapping images to produce interference fringes. The period of these fringes is a function of the absolute phase difference between the 2 segments.

To illustrate this, consider the field at the focus. Ignoring aberrations and diffraction and assuming equal segment illumination E_0, the field at the each point x along the detector dispersion axis is

$$E = E_0 \exp\left(\frac{2\pi i L}{\lambda(x)}\right)\left(1 + \exp\left(\frac{2\pi i dL}{\lambda(x)}\right)\right) \tag{1}$$

Ideally, the dispersing element would have a $1/\lambda$ characteristic, so that the field would vary as a cosine function whose period is everywhere proportional to dL. Using a grism placed in the filter wheel makes for a compact package, but nonideal dispersion characteristics, as the dispersion is nearly linear with λ:

$$\lambda = \alpha_x x + \lambda_0 \tag{2}$$

The intensity pattern that results is

$$I = 2E_0^2\left(1 + \cos\left(\frac{2\pi dL}{\alpha_x x + \lambda_0}\right)\right) \tag{3}$$

The period can be measured as a function of x and matched to Eq. 3 to determine dL. The sign of dL is determined by moving the outer segment a small amount and repeating the measurement. Then the segment is moved to its nominal position in a single step.

The DFS has a large dynamic range. The maximum detectable OPD difference is defined by the Nyquist sampling limit of the particular detector and the dispersion of the grism or prism. This will nominally be set to be larger than the focal depth of the segments, as greater OPDs can be easily detected and corrected by simple focus scan techniques. Aberrations, including defocus, will tend to reduce the visibility of the interference fringes, but with many of them spread out across the detector this is not expected to be a significant problem. Alignment of the grism to the detector may be done following the alignment of the central segment, using narrow-band filters to register particular wavelengths on the detector.

Use of the DFS allows pairwise phasing to within a wave in just a few actuation steps. This phasing approach is in routine use at the Palomar Testbed Interferometer, where it is used to phase up widely-separated small apertures using starlight.
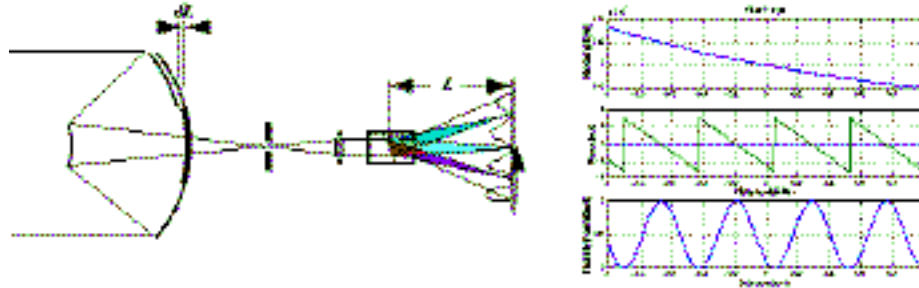
Figure 9. Dispersed-fringe sensor.

The coarse phasing of segment pairs may conclude with a "direct image-sharpening," or "white-light interferometry" (WLI) step[7]. Following the setting of the outer segment using the DFS, the DFS is removed from the beam by rotating the filter wheel, so that the detector once again sees a star image. The outer segment is then scanned in piston, and the position with the highest peak intensity is identified. The segment is moved back to that point.

If the DFS is used, the starting point for the image sharpening step will be rather good, and a single step of image sharpening should yield excellent segment-to-segment phasing accuracy, within WF precision set by the segment figure quality. If the DFS is not used, the starting point may not be as good. If the initial error is many waves, piston will have to be scanned over a long range. The coherence of the 2 spots depends on the bandpass of the filter and source that produces the image. the peak intensity oscillates at the half-wavelength scale, within an envelope defined by the bandpass of the source/filter used. The sharpest peak represents the white-light fringe, and occurs at the ideal in-phase point. For long piston scans, the angular alignment will need to be readjusted, by scanning in tip and tilt to assure best coalignment of its spot with that of the central segment.[7]

At this point, coarse phasing of the first outer segment to the central segment is complete. The coarse phasing process is then repeated for the next segment. This can be done pairwise, with respect to the central segment, by tilting the previously-aligned segment back out of the way, or it can be done relative to the multi-segment aperture composed of the central segment and all previously-aligned segments. The best approach is being explored.

When all segments have undergone coarse phasing, and all are brought back into alignment with the central segment, the PM will be aligned and phased to within a wave – well within if the segment figure quality and the actuator accuracy are good.

The computer processing required for most phases of the coarse figure control is within the capabilities of an on-board computer. The degree to which human intervention is required or desirable is being explored. It is possible that most of this procedure can be run autonomously on-orbit.

5.FINE FIGURE CONTROL

Fine Initialization Control picks up where the Coarse Initialization leaves off: with the PM segments, SM and ISIM phased to within about a wave. The fine figure control phase adjusts the segment position and

orientation slightly, and then sets the 349 actuators of the continuous face-sheet DM to minimize WF error. The result is a diffraction limited telescope at 2 um wavelength.

As with the coarse figure controller, all sensing is performed using the Near IR Camera. Focus-diverse imagery is required, and will be effected by a piston mirror within the SIM Near-IR camera. The required processing is substantial and will likely be performed on the ground, with the resulting segment and DM control commands are uplinked for implementation on the spacecraft.

Fine figure control proceeds in 2 distinct phases: wavefront sensing; and wavefront control.

Wavefront sensing is performed using focus-diverse, iterative transform phase retrieval.This starts by taking two or more images, defocussed enough to spread the light over a large number of pixels (20-200, depending on required sensitivity and desired spatial frequency resolution). Typically 3 images, one in focus and 2 taken on opposite sides of focus, are used. These images are processed using a modified Gerchberg-Saxton algorithm[10], as sketched on Fig. 10. The G-S iteration starts with a random guess at the phase of the pupil used to form the image. This is combined with the square-root of the amplitude of the image data to create an estimate of the image. This is inverse Fourier transformed back to pupil space, and then the phase due to the diversity factor (the defocus) is removed, and the aperture mask is applied. The result is an estimate of the in-focus pupil. Then the diversity factor is put back in and the result is Fourier transformed back to the image plane. The phase from this estimated image-plane field is combined with the square-root of the data to start the next iteration.
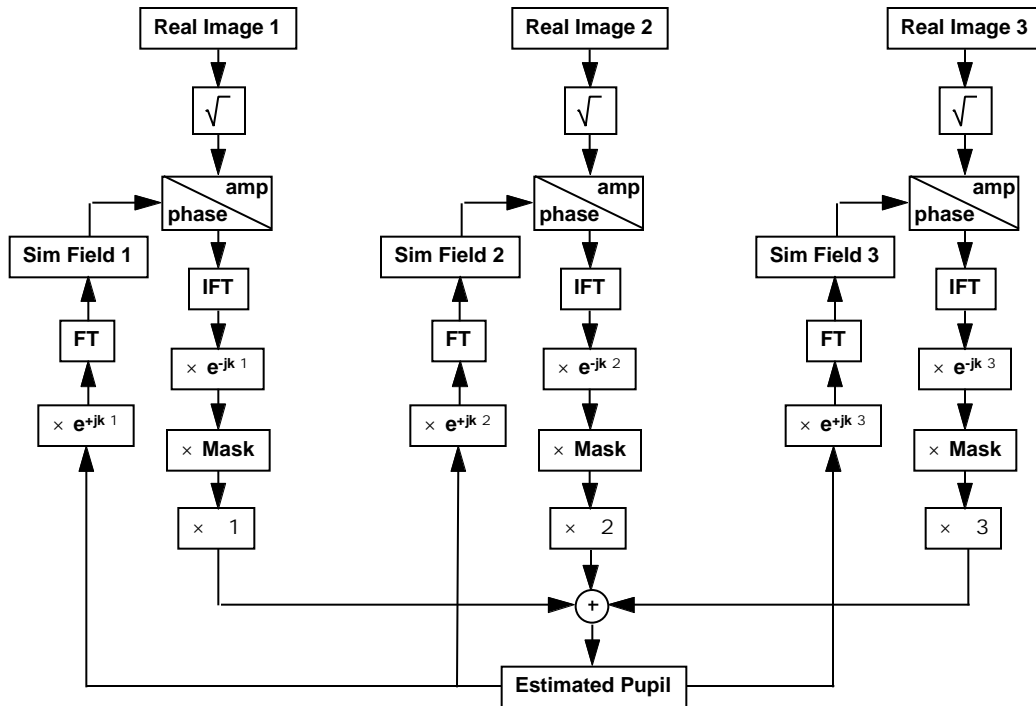

**Figure 10. Focus-diverse iterative-transform phase retrieval algorithm.**

About 10 of the G-S iterations are performed for the first image before moving to the next and repeating. The pupils estimated by iterating on each image are weighted and then combined to generate a joint estimate of the in-focus pupil wavefront. The entire process is repeated, typically 20-40 times, until the differences between iterates is below a low threshold.

An example case is shown in Figs. 11 and 12. Here small random segment figure errors, along with small misalignments of all of the optics, were introduced into the NGST Yardstick computer model. Simulated images were generated at 3 focus positions: in-focus, and ±100 um equivalent SM piston to induce defocus. Photon noise was added assuming the image went to full well at 80,000 photoelectrons, with a 12 bit readout. Read noise of 10 photoelectrons was also included. Pixel sampling is 27 um. These "real" images

9

are shown in the top row of Fig. 11, along with the in-focus pupil generated from the model, which is not known to the controller.
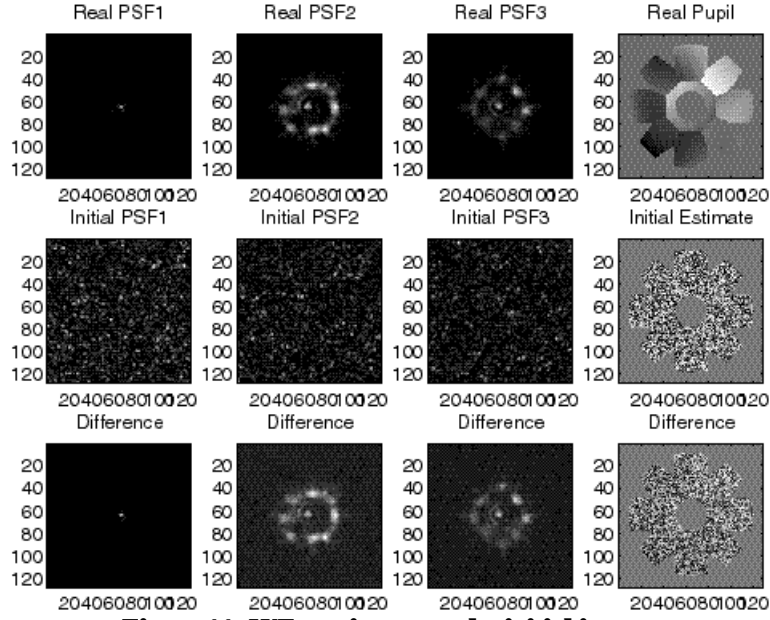
Figure 11. WF sensing example: initial iterate.
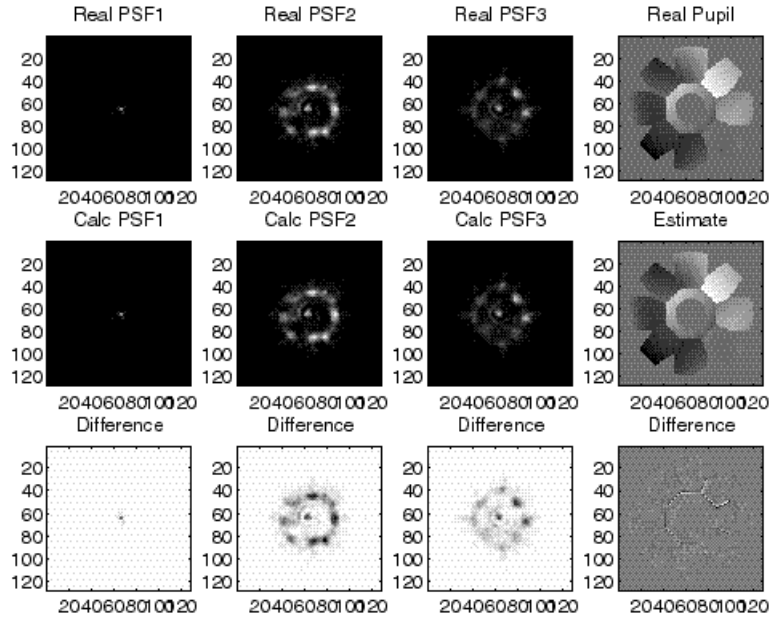
Figure 12. WF sensing example: final iterate.

The iteration was set up to use a 2x oversampling, to avoid wrap-around and aliasing problems in the Fourier transforms. The initial guess is shown in Fig. 11, middle row, along with the initial image estimates generated from it. The initial match is poor, but improves rapidly as the algorithm runs. The final estimate is shown in Fig. 12. In this case, 20 iterations were run, and the final error was 1/293 waves.

Experience indicates that running with a single image does not converge unless there is no noise. Use of an in-focus image can add more noise than information.

To determine overall wavefront sensing performance, various Monte Carlo simulations have been run. Results of 2 such are shown on Fig. 13. These illustrate the sensitivity of the estimated wavefront to camera

dynamic range and to camera read noise. They indicate that 12-14 bits will be adequate for dynamic range, and that the impact of 0-10 electrons read noise is quite small. Further tests are being run to quantify effects such as jitter, finite bandwidth, stray and scattered light, and other degrading factors.

Large WF errors require phase unwrapping, which is aided by repeating the wavefront sensing process at multiple wavelengths so as to resolve phase discontinuities. This slows the WF sensing process down but does not present a fundamental obstacle. The option exists to sense at quite long wavelengths – aberrations of a few waves at a sensing wavelength of 5 or 10 um should be easily measured, providing a sensing capability of 20-50 waves at HeNe.

Other wavefront sensing methods will also be analyzed. These include phase retrieval using other algorithms and other diversity factors, such as wavelength.[11] Phase diversity algorithms, which offer the potential for a continuous WF sensing mode will be studied.[12] Use of separate interferometric WF sensor of Mach-Zender or rotation shearing type offer interesting scientific as well as control options and will be studied.[13] Shack-Hartman WF sensors, used in conjunction with segment edge sensors, are also possible. The DCATT testbed now being assembled at Goddard Space Flight Center will provide a versatile facility for demonstrating and testing WF sensing and control performance, and will provide means to confirm the performance predicted by simulation studies.[14]
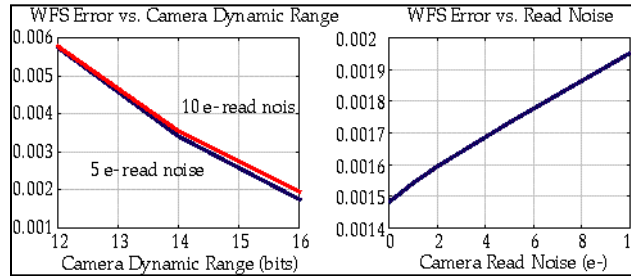
Figure 13. WF sensing performance vs. read noise.

The wavefront control phase of fine figure initialization takes the estimated wavefront and uses it to determine new actuator commands for the segments, the SM and for the DM. The wavefront estimate is interpolated to a grid of 1856 discrete points in the pupil, corresponding to about 6 points per DM actuator. This interpolated estimate is vectorized and is designated w. The wavefront w is – for small motions – a linear function of the optical states x, which in the Yardstick model includes 3 rotation and 3 translation degrees of freedom per optic, plus 45 Zernike deformation terms per segment, plus 1044 structural finite-element model nodes on the surface of the segments and at the centers of rotation of each of the other optics. It is also a function of the control vector u, which includes 3 to 6 DOF per segment, plus 349 DM actuators. The linearized model of w takes the form:

$$w = \frac{dw}{dx}x + \frac{dw}{du}u \tag{4}$$

The control seeks to minimize the cost function J, the wavefront error squared:

$$J = \frac{1}{2}w^T w \tag{5}$$

The least-squares solution for the next control step is

$$u = -G\bar{w} = -\left[\frac{dw}{du}^T \frac{dw}{du} \right]^{-1} \frac{dw}{du}^T \bar{w} \tag{6}$$

The error remaining in the wavefront includes the error in the wavefront estimate $\bar{w}$, actuation error q, which is a zero-mean random process with covariance Q, and effects of limited spatial resolution and other constraints on the solution, captured in the fact that the matrix $[I – (dw/du)]$ 0. For larger initial errors x linearity error becomes a factor: for initial displacements more than a few hundred microns, the segment control typically needs 2 or 3 iterations to converge. In practice, this may require 2 or 3 cycles of wavefront sensing/wavefront control, with images taken, actuators moved, then more images taken, actuators moved again, etc.

Errors in the estimate can be treated as noise r, with zero mean and covariance R:, so that:

$$\bar{w} = w + r \tag{7}$$

The wavefront error post-control is:

$$dw = \left[I - \frac{dw}{du}G\right]w + \frac{dw}{du}Gr + \frac{dw}{du}q \tag{8}$$

The covariance of this residual error, written W, is:

$$W = \left[\frac{dw}{dx} - \frac{dw}{du}G\frac{dw}{dx}\right]X\left[\frac{dw}{dx} - \frac{dw}{du}G\frac{dw}{dx}\right]^T + \frac{dw}{du}GR\frac{dw}{du}G^T + \frac{dw}{du}Q\frac{dw}{du}^T \tag{9}$$

Here X is the covariance of the state, including each the misalignment and figure error of each optic (assumed zero mean). The expected value of the RMS wavefront error is:

$$WFE = \sqrt{\mathbf{trace}(W)} \tag{10}$$

There are a couple of different ways to predict WFS/WFC performance, given statistics X on the state x. Full nonlinear Monte Carlo simulation uses the statistics of the state and the measurement and actuator errors to realize a large number of separate cases, which are then simulated, with the results recorded for analysis. This approach encompasses the nonlinearities that appear with large errors.

Covariance analysis uses Eq. 9 to directly propagate the covariance matrices, so that the statistics of the post-control residuals can be computed in a single step, rather than performing analysis on a large number of simulated cases. Covariance analysis is strictly linear method, however. Both methods are applied in the sections that follow.

The wavefront estimate computed in the example of Figs. 11 was used to compute control commands. First segment control only commands were computed. When applied, these reduced the error from 320 nm to 66 nm, as illustrated in Fig. 14. Then the DM control was applied, further reducing the WFE to 21 nm. Final SR was 1.0.

Experience with WF control of the simulated Yardstick shows that the optimal control moves the segments to reduce wavefront error, but not necessarily to minimize it. The segment control, which is computed with knowledge of the continuous face-sheet DM, sacrifices some WFE performance to minimize edge discontinuities. The continuous facesheet DM then becomes much more effective, yielding lower overall WF error.

The remaining sections of this paper address the effectiveness of the control system outlined above in compensating significant error sources expected for NGST.
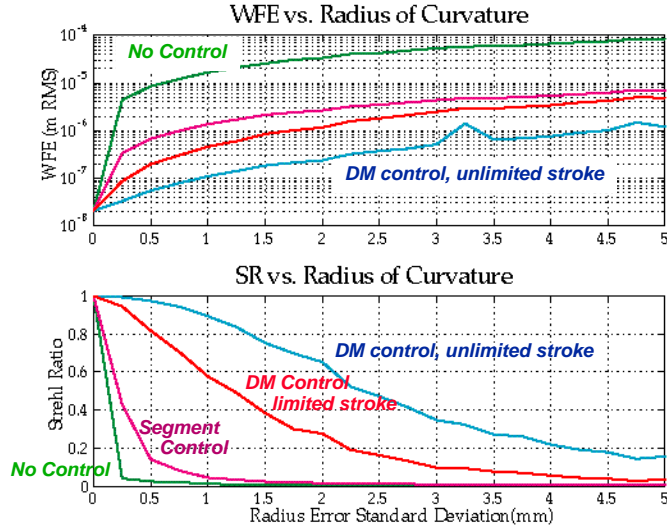
6.MIRROR FIGURE ERRORS

There are several different sources of primary mirror segment figure errors, including imperfect fabrication, ground-to-orbit temperature changes, temperature changes between different observing attitudes, gravity relief, and dimensional stability factors such as desorption. The WF control system deals with these in the same fashion, irrespective of origin. In this section, a general form for low-order figure errors – from whatever cause – is applied to explore sensitivities and develop a preliminary closed-loop error budget. Alignment errors and thermal errors are dealt with specifically in later sections.

First consider the effect of changing radius of curvature between the individual segments. Fig. 15 shows the effect on WFE for 4 cases. The "no control" curve shows how performance degrades with increasing error if no realignment of WF control is used – not really an interesting case. The next curve shows performance if the segments are controlled, but without using the DM. To maintain 80% SR it is seen that radius must be controlled to about 100 um. The best case is for segment and DM control, with unlimited DM stroke. The 80% SR point is about 10 times better than the segment-control-only case, allowing over 1.3 mm RoC error. Applying a ±2 um stroke limit drops the tolerance back to 0.5 mm – still a substantial improvement over the segment control case. Further improvement would require more DM actuators, or direct bending of the PM segments to reduce edge discontinuities.
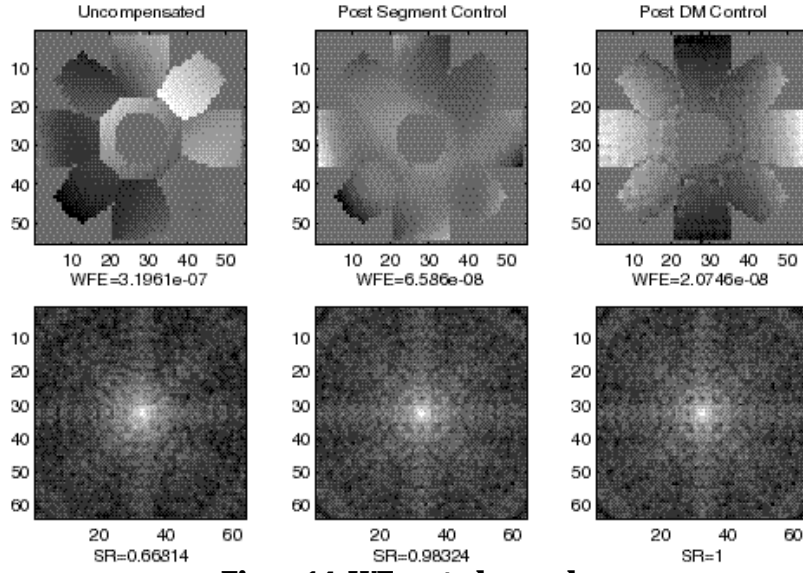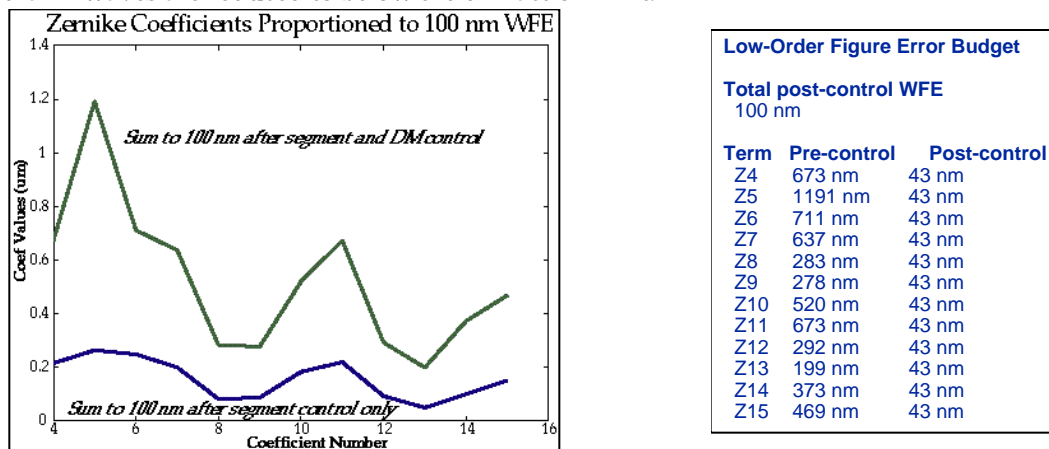
Figure 14. WF control example.

Figure 15. Sensitivity to segment radius of curvature.

Next consider figure errors in terms of Zernike polynomials, centered at the vertex of the full PM, but varied independently on each separate segment. The polynomials are normalized on the full NGST aperture, but are not orthonormal, due to the scalloping at the edge of the aperture.

Monte Carlo performance as a function of Zernike coefficient standard deviation, computed on the same basis as for the radius case above, is shown in Fig. 16. This chart summarizes the segment-control-only performance and the stroke-limited performance on a term-by-term basis. Monte Carlo response curves like those of Fig. 15 are generated for each Zernike polynomial in turn. These are then interpolated to find the error levels that give a contribution of 43 nm (including the 20 nm nominal WFE) to the overall WF error. The numbers plotted are the values of the coefficients that sum to a total of 100 nm post segment control or post limited DM control, as indicated.

A preliminary budget for the low-order figure errors is also shown on Fig. 16, showing substantial term-by-term reduction of the pre-control error by the control system. The WF control system is effective in

13

reducing figure errors regardless of source. Depending mainly on gap discontinuities, figure errors of more than 2 waves are reduced to below the diffraction limit.

Low-Order Figure Error Budget

Total post-control WFE
100 nm

Term	Pre-control	Post-control
Z4	673 nm	43 nm
Z5	1191 nm	43 nm
Z6	711 nm	43 nm
Z7	637 nm	43 nm
Z8	283 nm	43 nm
Z9	278 nm	43 nm
Z10	520 nm	43 nm
Z11	673 nm	43 nm
Z12	292 nm	43 nm
Z13	199 nm	43 nm
Z14	373 nm	43 nm
Z15	469 nm	43 nm

Figure 16. Sensitivity to low-order figure errors.

Final NGST figure error budgets will include full accounting for environmental effects and the mitigation available from WF control. A reasonable objective is to set the low-mid frequency WF error ballocation such that the dominant term is the error from thermal deformations. This error should be minimized by use of cryo-null figuring, good thermal and structural design, and other factors – but there will be some unavoidable residual figure error at operating temperatures. All other terms in the figure error budget should be made lower than this, if possible, and the WF control system should be optimized to remove all of these effects together. It may be important from a cost and schedule viewpoint that mirror figure quality not be over-constrained, when environmental factors will likely dominate the WF budgets.

7.ALIGNMENT ERRORS

Post-launch, post-deployment optical alignments can be expected to be poor, as discussed above. In this section, the contribution to post-WF control wavefront error is examined. In this case we use covariance analysis, following Eqs. 9 and 10, rather than Monte Carlo analysis, to obtain general results.

Figure 17 shows WF performance over a very wide range of possible deployment errors. Here "deployment" error is any effect that translates or rotates any of the PM optics. The x-axis shows the deployment error standard deviation. This is really the value of the uniformly distributed standard deviation of each of the 6DOF error terms for each of the 9 segments. The y-axis shows the WFE for each of the various curves.

The upper curve shows the uncontrolled response of the system: WFE goes linearly with deployment error. The next curve down shows the effect of (3DOF) segment control only. It hits a noise floor set by the variance of the segment actuators. The lowest curve shows the effect of segment and DM control; it is about 10x lower than the segment control only curve.

The lowest noise floor is labeled "DM noise floor," but it is actually set by the segment actuator noise level. It has to do with the amount of segment edge discontinuity left in the pupil. These discontinuities are difficult for the DM to counter. The optimal controller knows this, and actually drives the segments to minimize edge discontinuities, letting the DM clean up the bulk figure errors. This noise floor can be lowered by using more DM actuators. Performance with 6DOF of control per segment is set by the noise floors only. With expected WF sensing performance and no mirror figure errors, the ultimate determinant of WF performance is the segment actuator accuracy. In the case of 80 nm and 80 nrad segment actuation error performance, with 6DOF control, WF error is reduced from arbitrary initial values to 50 nm RMS, well within the budget.

Raw and Compensated Wavefront Error

RMS WFE (m)

Deployment Error Sigma (m and rad)
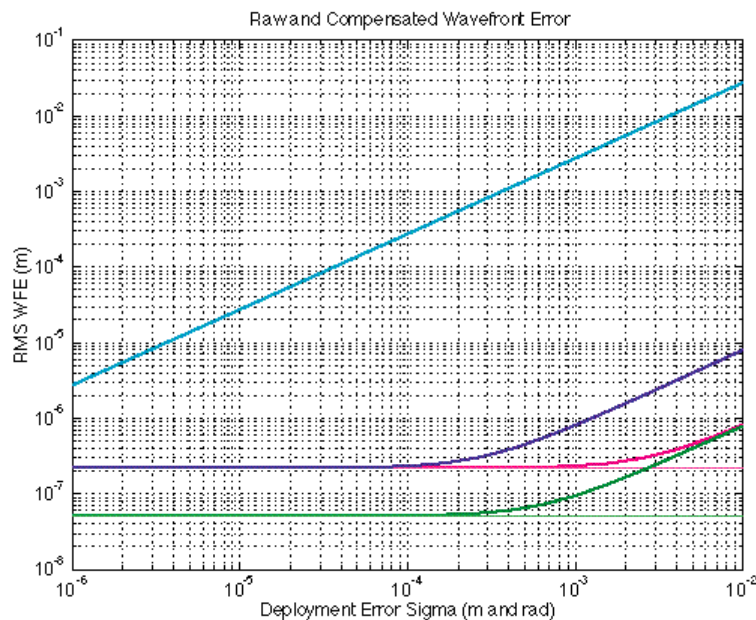
NGST 8-Petal configuration
8 meter aperture
F/1.25 primary
F/24 system
 = 1.0 μm (0% bandpass)
Random initial segment state errors
Optimal WF controller
Set DM and segments together
Follow up with DM only
Phase sensing
Results via covariance analysis

Deployment error in 6DOF
Uniform variance
Segment actuation in 3DOF
Segment actuation error 8e-8 rad & m
DM actuation error 1e-9 m
Sensing error 1e-12 m

Figure 17. Alignment performance.

8. THERMAL DEFORMATIONS

Cryogenic operation presents a major challenge for NGST, and one of the main areas of concern is here in the thermal deformation of the optics as they go from the test enviroment to on-orbit conditions. This section addresses the changes that the Yardstick experiences as it cools, and then again, as it changes attitude during observations. Figure 18 indicates the temperatures expected in operation at L2.
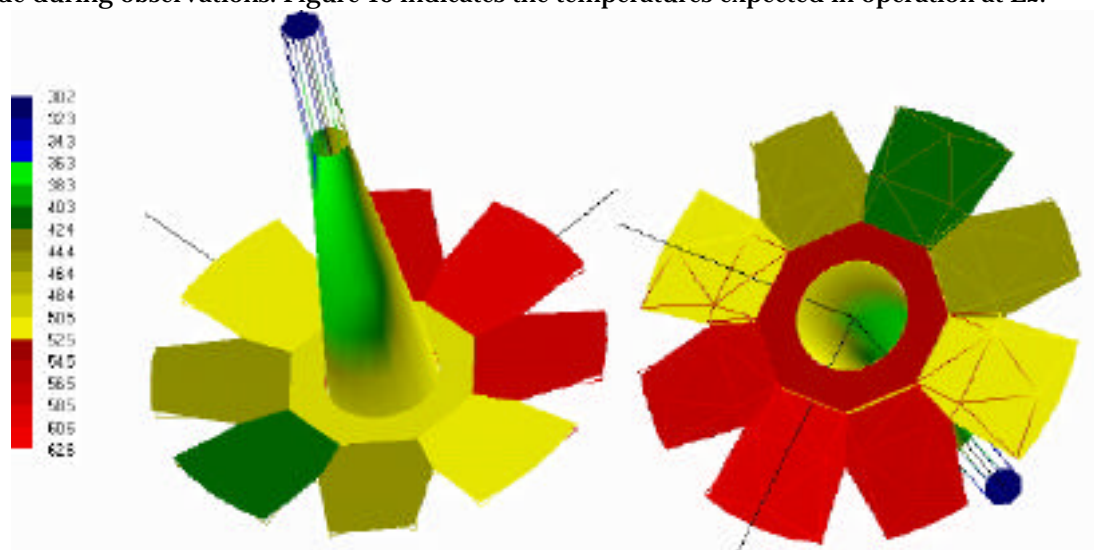

Figure 18. Temperatures at operating conditions.

NGST will use cryo-null figuring to establish the final figure of its optics. Tested successfully by the SIRTF program, this process uses testing at near-operational temperatures, along with room-temperature polishing, to achieve final figure. The final segments will have figure errors built in that compensate the warping that occurs in cooling, so that at operating temperatures, they are of excellent quality.

Figure 19 shows what happens to optics that are perfect at 100°K when they are cooled to the temperatures on Fig. 18. Initial WFE is 46 microns. After segment-only WF control in 3DOF, this error is reduced to 240

nm. Most of this control has acted to counter "rigid-body" motions of the segments. The DM is effective in restoring full performance, though the DM stroke limit (1.8 um) brings the WF error back up to 77 nm.
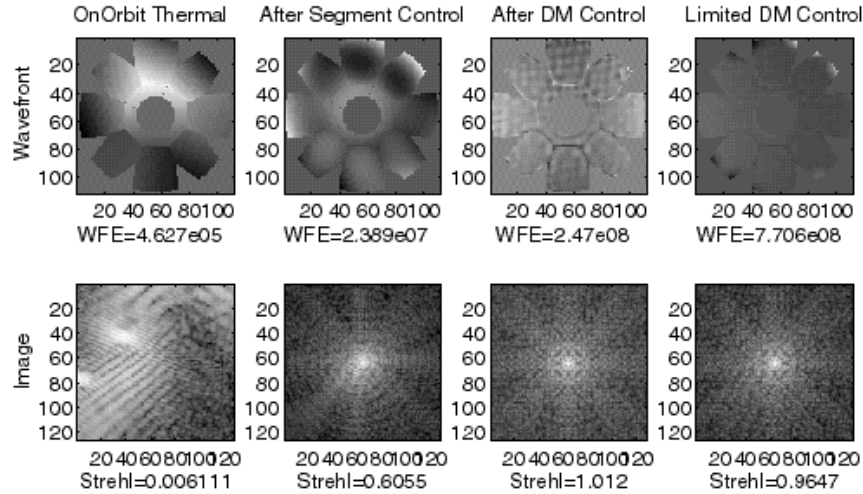
Figure 19. Ground-to-orbit thermal response, pre- and post-control.

Performance during an observation period is shown on Fig. 20. Here initial mirror figure errors and misalignments were compensated by the WF control system, yielding a post-initialization SR of about 0.8 at 2 um wavelength. Then the spacecraft is slewed from the hot extreme on-orbit to the cold extreme, which results in temperature changes in the OTA of up to 2 °. These changes take place over 27 hours following the 1 hour slew. Final SR is 0.7. Figure 21 summarizes the performance vs. time.
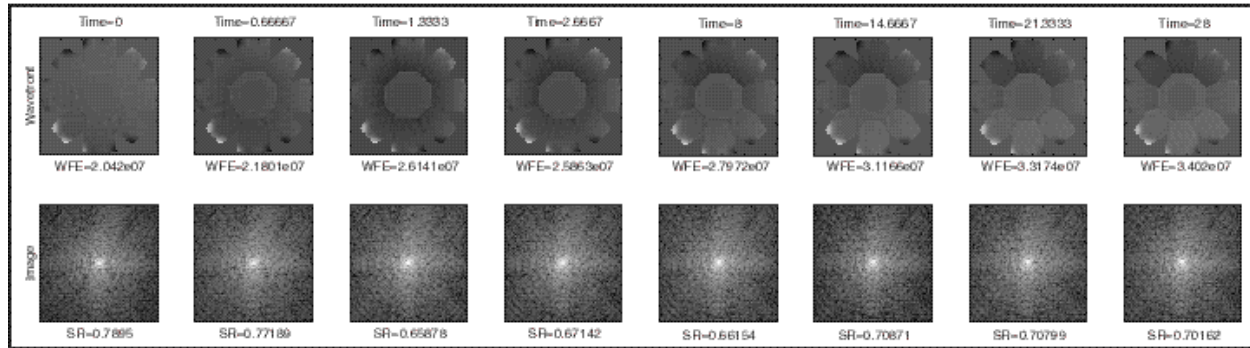
Figure 20. Transient thermal response, worst-case slew.

9. CONCLUSION

The baseline NGST optical control system described here is shown to be effective in increasing tolerances to mirror figure errors, structural misalignments, and thermal deformations many-fold. The wavefront control system takes the place of the massive, stiff structure traditionally utilized to preserve alignments and optical quality. By providing a high degree of on-orbit adjustability, the WF control system dramatically reduces requirements on structural and thermal stability and mass, allowing NGST to break the traditional telescope cost paradigm.

10. ACKNOWLEDGEMENT

11. REFERENCES

1. B. D. Seery, "Next generation space telescope (NGST)," Paper 3356-01, Kona HI (1998).

2. J. C. Mather, E. P. Smith, H. S. Stockman, "Scientific metrics for the next generation space telescope," Paper 3356-02, Kona HI (1998).

3. G. E. Mosier, M. Femiano, K. Ha, P. Y. Bely, R. Burg, D. C. Redding, A. Kissil, J. Rakoczy, L. Craig, "Integrated modeling environment for systems-level performance analysis of the next generation space telescope," Paper 3356-08, Kona HI (1998).

4. D. Redding, P. Dumont and J. Yu, "Hubble Space Telescope Prescription Retrieval," Applied Optics, Vol. 32, No. 10 (1993).

5. D. Redding, A. Boden, S. Sirlin, J. Mo, R. Hanisch and L. Furey, "Optical Prescription of the HST," *Calibrating Hubble Space Telescope: Post Servicing Mission*, Space Telescope Science Institute (1995).

6. S. Sirlin and D. Redding, "VSIM," NASA Tech Briefs (1997).

7. S. Sirlin and D. Redding, "Modeling and Initialization of a Segmented Telescope," *Controls for Optical Systems*, SPIE 1696, pp. 243-252 (1992).

8. A.E. Bryson and Y.C. Ho, *Applied Optimal Control*, Halsted Press, 1969.

9. J. B. Hadaway, , M. E. Wilson, NASA Goddard Space Flight Ctr.; , D. C. Redding, R. A. Woodruff, "Lessons learned in the optical design of the next generation space telescope," Paper 3356-75, Kona HI (1998).

10. R.W. Gerchberg and W.O. Saxton, "A Practical Algorithm for the Determination of Phase from Image and Diffraction Plane Pictures," Optik 35, 237-246 (l972).

11. J.N. Cederquist, J.R. Fienup, C.C. Wackerman, S.R. Robinson and D.Kryskowski, "Wave-Front Phase Estimation from Fourier Intensity Measurements," J. Opt. Soc. Am. A 6, 1020-1026 (1989).

12. R.G. Paxman, T.J. Schulz and J.R. Fienup, "Joint Estimation of Object and Aberrations Using Phase Diversity," J. Opt. Soc. Am. A 9, 1072-85 (1992).

13. R. Burg, P. Y. Bely, L. Petro, J. Gay, Y. Rabbia, P. Baudoz, D. C. Redding, "Searching for exo-zodiacal discs with an interferometric coronagraph," Paper 3356-33, Kona HI (1998).

14. C. LeBoeuf, P. S. Davila, D. C. Redding, D. R. Coulter, L. Pacini, "Deployed cryogenic active telescope testbed (DCATT): a wavefront sensing and control testbed for the next generation space telescope (NGST), Paper 3356-72, Kona HI (1998).

15. A. E. Lowman, S.A. Macenka, D. C. Redding, S. A. Basinger, "Infrared telescope technology testbed primary mirror test results," Paper 3356-44, Kona HI (1998).
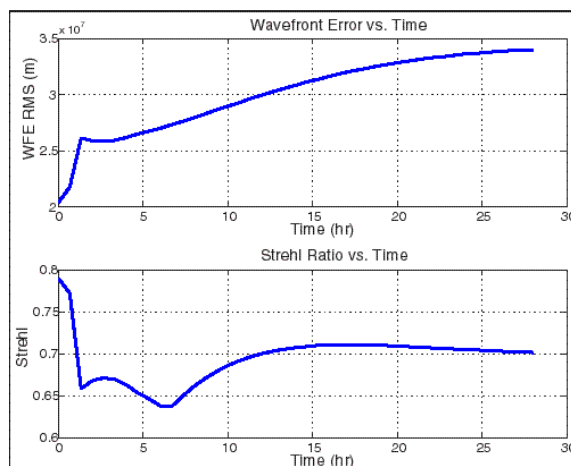
Figure 21. Transient thermal response summary, worst-case slew.